Aerospace Science and Technology 144 (2024) 108808

Contents lists available at ScienceDirect

Aerospace Science and Technology

journal homepage: www.elsevier.com/locate/aescte

Computational aeroelastic analysis of wings based on the structural discontinuous Galerkin and aerodynamic vortex lattice methods

Vincenzo Gulizzi *, Ivano Benedetti *

Department of Engineering, University of Palermo, Viale delle Scienze, Edificio 8, Palermo, 90128, Italy

ARTICLE INFO

Communicated by Damiano Casalino

Keywords:
Computational aeroelasticity
Discontinuous Galerkin method
Higher-order structural modelling
Vortex lattice method

ABSTRACT

An original computational framework for the aeroelastic analysis of wings featuring general transverse section is developed. The framework is based on the coupling between a novel discontinuous Galerkin structural model and an aerodynamic vortex lattice method, which is implemented in both the planar and non-planar version. The structural model, which constitutes the novelty of the present work, allows generalized kinematics and is thus able to capture higher-order structural deformation modes. With respect to other more used structural representations, the discontinuous Galerkin approach is based on the use of discontinuous basis functions and suitably-defined boundary terms to enforce the inter-element continuity and boundary conditions. Such features naturally enable high-order accuracy, ease of parallelization and, specifically for this work, straightforward coupling with the vortex lattice method. The framework is validated through benchmark tests, providing favourable matching with reference literature data.

1. Introduction

The capability of predicting the response of structures or structural components subject to the action of aerodynamic flows is of crucial importance for several technological applications, in sectors as diverse as civil, energy, automotive or aerospace engineering. *Aeroelasticity*, which provides a systematic approach to the analysis of problems involving the interaction of elastic, inertial and aerodynamic loads, constitutes a core discipline in civil and aerospace syllabi and it is employed for the construction of suspended bridges [1], high-rise buildings [2], wind turbines [3] and aircraft components [4]. In the most benign cases, poor aeroelastic design may result in the degradation of the performance of the structure with respect to its intended purpose, while it may critically affect its safety, leading to catastrophic outcomes, in the most serious cases [5–7].

In aeronautics and aerospace engineering, aeroelastic considerations enter the initial stages of conceptual design and often constitute a key factor affecting several subsequent design choices. Aeroelastic stability requirements for transport category airplanes are listed for example under Title 14 CFR §25.629, which requires that compliance with the requirements set forth in there *must be shown by analyses, wind tunnel tests, ground vibration tests, flight tests, or other means found necessary by the Administrator*. Aeroelastic considerations are particularly important for modern high-altitude long-endurance (HALE) aircraft that, to achieve their desired flight performance, typically feature high aspect ratio wings, prone to significant aeroelastic deformations due to their high flexibility.

In aeroelastic design, it is then important, for designers and companies, to be capable of assessing the aeroelastic behaviour of the considered structural configurations quickly and effectively, since the very preliminary stages of design, when the main structural arrangements are to be selected and the employment of highly refined analysis tools might result unduly costly and time consuming. In this context, the availability of fast, robust, accurate and reliable computational tools, with reasonable predictive capabilities, constitute an important industrial asset, especially when the design space is broad and offers different alternatives for the fulfillment of certain purposes. This happens, for example, in modern aerospace structural design, where the availability of composite materials offers the designer a plethora of different choices, which may be too burdensome to be assessed through experimental testing only.

Such considerations motivate the interest in the research and development of novel computational tools for effective and accurate aeroelastic analysis. Indeed, different approaches for the analysis of structures under aerodynamic loads have been proposed in the literature, which may be classified based on the models adopted for describing both the

* Corresponding authors.
E-mail addresses: vincenzo.gulizzi@unipa.it (V. Gulizzi), ivano.benedetti@unipa.it (I. Benedetti).

https://doi.org/10.1016/j.ast.2023.108808
Received 5 October 2023; Received in revised form 16 November 2023; Accepted 3 December 2023
Available online 7 December 2023

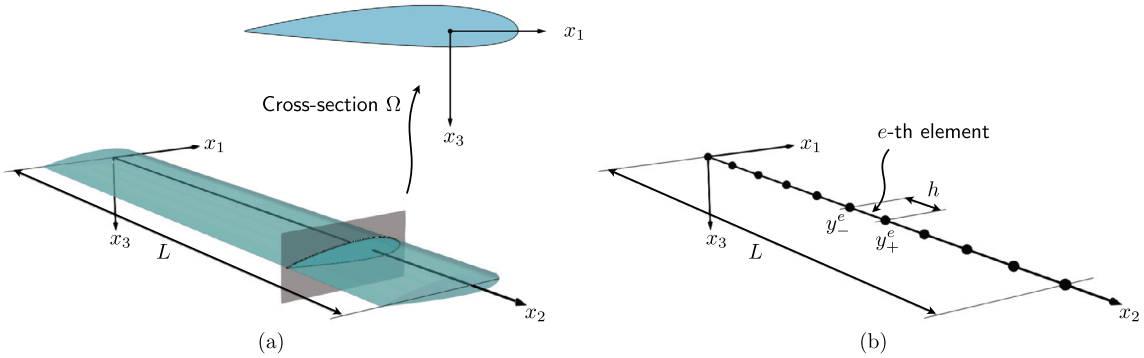

Fig. 1. (a) Sample wing modelled as a beam structure with length L and cross-section Ω. (b) Discretization of the wing in one-dimensional elements of size h.

structure and the aerodynamic field. In general, aeroelastic analyses fall within the class of fluid-structure interaction (FSI) problems and require the three-dimensional solution of fully coupled structural dynamics and fluid dynamics problems. Suitably coupled computational structural dynamics (CSD) and computational fluids dynamics (CFD) solvers have been used to investigate the aeroelastic response of bridges [8], helicopter and wind turbine blades [9,10], and high aspect ratio wings [11] among other applications. Such CFD-CSD approaches generally couple the finite element method (FEM) for structural analysis with different kinds of high-fidelity CFD models and tend to produce high-resolution results at considerable computational cost in terms of both storage and time, especially when fully three-dimensional representations are employed, which hinders their use for preliminary design purposes.

However, depending on the features of the structures being analysed, different kinds of structural idealisations may be adopted, with the aim of reducing the overall cost of the analysis [12,13]. Generalised shell elements for aeroelastic analysis [14] have been developed, and higher-order equivalent plate models have been coupled with CFD for aeroelastic analysis of complex aircraft wing structures [15,16]. Beam models have been used in conjunction with CFD for the aeroelastic analysis of slender solids, e.g. helicopter rotor and wind turbine blades [17,18] or high aspect ratio wings [19]. In such CFD-based aeroelastic models, when idealised structural models are used, the computational cost of the structural analysis becomes a small fraction of the overall analysis cost. For such a reason, different reduced order modelling (ROM) strategies have been developed in the literature to reduce the cost of the aerodynamic computations, while maintaining reasonable accuracy [20–22]. Such methods are particularly recommended when complex aerodynamic conditions need to be evaluated at reduced cost with respect to brute force CFD.

Less costly approaches resort to the use of beam or plate/shell structural models coupled with low /medium- fidelity aerodynamic models, such as the *vortex lattice method* (VLM), see e.g. Refs. [23–26]. Despite being limited to specific flow regimes (low-speed, high-Reynolds attached flow) [27], this approach offers fast numerical estimates of the aerodynamic loads on lifting surfaces.

The work presented here falls within the last class of models and focuses on the development of a novel framework for the aeroelastic analysis of wing structures based on the combined use of an Interior Penalty discontinuous Galerkin (DG) method for wing structures and a non-planar VLM using ring vortices. The novelty consists in the employment of a recently developed DG method for beams with general cross-sections [28] that allows using variable-order polynomial basis approximations for the structural analysis, enabling high-order accurate solutions for the wing problem. On the other hand, the ring-based VLM allows representing either flat or curved lifting surfaces. Numerical results are presented for wings featuring flat-plate or thin-walled NACA profiles and their comparison with available literature reference data demonstrates the potential of the proposed approach for fast numerical conceptual design assessment.

The paper is organized as follows. Section 2 presents the DG formulation adopted for the analysis of wing structures. The fundamentals of the aerodynamic VLM are recalled in Section 3, while the adopted aeroelastic coupling is detailed in Section 4. Eventually, the results of the performed computational tests are reported and discussed in Section 5. A general discussion about the merits, limitations and possible developments of the presented technique is reported in Section 6, before drawing few *Conclusions*.

2. Structural model

A wing with span L, referred to a global reference system $Ox_1x_2x_3$, whose origin is placed at the wing root section, is considered. The reference system is oriented so that the coordinates x_1 and x_3 span the wing cross-section and the axis x_2 is oriented along the span, see Fig. 1a.

2.1. Basic equations

The structure is assumed to undergo small strains and its response to remain in the linear elastic regime, with displacements represented by the vector $\boldsymbol{u} = \{u_1, u_2, u_3\}^\intercal$ and strain and stress components collected, in Voigt ordering and notation, within the vectors $\boldsymbol{\gamma} = \{\gamma_{11}, \gamma_{22}, \gamma_{33}, \gamma_{23}, \gamma_{31}, \gamma_{12}\}^\intercal$ and $\boldsymbol{\sigma} = \{\sigma_{11}, \sigma_{22}, \sigma_{33}, \sigma_{23}, \sigma_{31}, \sigma_{12}\}^\intercal$ respectively. It is also assumed that the wing is subjected to body forces acting over its volume V and surface tractions acting over S_t, whose components are collected within the vectors $\bar{\boldsymbol{b}} = \{\bar{b}_1, \bar{b}_2, \bar{b}_3\}^\intercal$ and $\bar{\boldsymbol{t}} = \{\bar{t}_1, \bar{t}_2, \bar{t}_3\}^\intercal$ respectively. The strain-displacement relationships, the linear elastic stress-strain constitutive relationships, and the indefinite equilibrium equations read as

$$\boldsymbol{\gamma} = \mathscr{D}\boldsymbol{u}, \qquad \boldsymbol{\sigma} = \boldsymbol{C}\boldsymbol{\gamma}, \qquad \mathscr{D}^\intercal\boldsymbol{\sigma} + \bar{\boldsymbol{b}} = \boldsymbol{0}, \qquad \forall \boldsymbol{x} \in V, \tag{1}$$

where $\mathscr{D}$ is the strain-displacement linear differential matrix operator, and provide the strong formulation for the structural problem, when coupled with the set of essential and natural boundary conditions

$$\boldsymbol{u} = \bar{\boldsymbol{u}} \quad \forall \boldsymbol{x} \in S_u \qquad\qquad \boldsymbol{t} = \bar{\boldsymbol{t}} \quad \forall \boldsymbol{x} \in S_t, \tag{2}$$

where the over-bar denotes assigned quantities.

2.2. Generalized kinematic assumptions and structural theory

It is assumed that the wing aspect ratio is high enough to allow representing the wing structure as a beam of length L and cross section $\Omega(x_2)$. The beam, assumed as a structural representation of the wing, is modelled employing higher-order theories, as in the Carrera Unified Formulation (CUF) [29] or Generalized Unified Formulation (GUF) [14], based on the generalized kinematic assumption

$$\boldsymbol{u}(x_1, x_2, x_3) = \mathbf{Z}(x_1, x_3)\,\boldsymbol{U}(x_2), \tag{3}$$

which expresses the displacements field $\boldsymbol{u}$ as a summation of products between *known* 2D functions $Z_k\left(x_1, x_3\right)$, defined over the wing cross-sections, and *unknown* 1D functions $U_k\left(x_2\right)$, defined along the wing span. In Eq. (3), $\mathbf{Z}\left(x_1, x_3\right)$ is the $3 \times N_u$ matrix containing the known cross-section functions Z_k, where $N_u = \left(1+N_{u_1}\right)^2 + \left(1+N_{u_2}\right)^2 + \left(1+N_{u_3}\right)^2$ and N_{u_k} expresses the order of expansion of the displacement component u_k; it is worth noting that, in the present scheme, the expansion is performed in terms of tensor-product polynomials. On the other hand, the vector $\boldsymbol{U}\left(x_2\right)$ collects the unknown components of U_k, referred to as *generalized displacements*, which play the role of primary variables in the considered problem.

The differential governing equations for the adopted structural representation, expressed in terms of generalized displacements, are obtained by feeding the kinematic model in Eq. (3) into the statement of the *principle of virtual displacements* (PVD)

$$\int_V \delta\boldsymbol{\gamma}^\intercal \boldsymbol{\sigma}\,\mathrm{d}V = \int_V \delta\boldsymbol{u}^\intercal \overline{\boldsymbol{b}}\,\mathrm{d}V + \int_{S_t} \delta\boldsymbol{u}^\intercal \overline{\boldsymbol{t}}\,\mathrm{d}S, \tag{4}$$

which, upon integrating by parts, assuming the constitutive and strain-displacements equations given in Eq. (1), and integrating the known functions over the wing cross-section leads to

$$-\frac{\mathrm{d}}{\mathrm{d}x_2}\left(\boldsymbol{Q}\frac{\mathrm{d}\boldsymbol{U}}{\mathrm{d}x_2} + \boldsymbol{R}\,\boldsymbol{U}\right) + \boldsymbol{R}^\intercal\frac{\mathrm{d}\boldsymbol{U}}{\mathrm{d}x_2} + \boldsymbol{S}\,\boldsymbol{U} = \overline{\boldsymbol{B}} \quad \text{for } x_2 \in D \equiv [0, L], \tag{5}$$

with the generalized stiffness matrices are defined as

$$\boldsymbol{Q} \equiv \int_\Omega \mathbf{Z}^\intercal \boldsymbol{c}_{22}\mathbf{Z}\,\mathrm{d}\Omega, \quad \boldsymbol{R} \equiv \int_\Omega \mathbf{Z}^\intercal \boldsymbol{c}_{2\alpha}\frac{\partial\mathbf{Z}}{\partial x_\alpha}\,\mathrm{d}\Omega, \quad \text{and}$$
$$\boldsymbol{S} \equiv \int_\Omega \frac{\partial\mathbf{Z}^\intercal}{\partial x_\alpha}\boldsymbol{c}_{\alpha\beta}\frac{\partial\mathbf{Z}}{\partial x_\beta}\,\mathrm{d}\Omega. \tag{6}$$

In the above equations, the Einstein tensor notation is used, D denotes the modelling domain of the beam, $\alpha, \beta = 1, 3$, and $\boldsymbol{c}_{kl} \equiv \boldsymbol{I}_k^\intercal \boldsymbol{C}\boldsymbol{I}_l$, with $k, l = 1, 2, 3$, are 3×3 matrices collecting subsets of the elastic coefficients of $\boldsymbol{C}$, see, e.g., Ref. [30]. The generalized domain load stems from the body forces $\overline{\boldsymbol{b}}$ and the surface tractions $\overline{\boldsymbol{t}}$ acting on the lateral surface of the beam as

$$\overline{\boldsymbol{B}} \equiv \int_\Omega \boldsymbol{Z}^\intercal\overline{\boldsymbol{b}}\,\mathrm{d}A + \int_{\partial\Omega} \boldsymbol{Z}^\intercal\overline{\boldsymbol{t}}\,\mathrm{d}\partial A, \tag{7}$$

where $\partial\Omega$ denotes the contour of the cross-section of the beam.

It is worth noting that all the integrals extended over the cross section Ω of the beam, appearing in Eqs. (6)-(7), are computed through standard Gaussian quadrature, considering the specific geometric shape of the cross section itself. When airfoil cross sections are considered, the external shape is drawn employing the explicit generating functions or procedures, such as, for example, the camber line and thickness distribution functions associated with NACA airfoil families. This strategy allows the structural model to incorporate the information about the curvature and material distribution of the beam cross section, in the framework of the so-called equivalent beam/plate modelling, see e.g. [31,23–25,15,16].

2.3. Discontinuous Galerkin formulation

The set of differential equations given in Eq. (5) is solved using an Interior Penalty discontinuous Galerkin approach for beam structures [28], which belongs to a recently-developed class of DG-based solvers for various structural components, such as beams, plates and shells [32, 30,33–35].

The modelling domain D of the beam is divided into N_e non-overlapping elements, i.e. $D \approx D^h \equiv \bigcup_{e=1}^{N_e} D^e$, where D^e is a generic e-th element.

The space $\mathcal{V}^{hp}$ of discontinuous basis functions is introduced as

$$\mathcal{V}^{hp} \equiv \{v : D^h \to \mathbb{R} \mid v(x_2 \in D^e) \in \mathcal{P}^p(D^e)\ \forall e = 1, \dots, N_e\}, \tag{8}$$

where $\mathcal{P}^p(D^e)$ is the space of polynomials up to degree p defined over the element D^e. Then, it is possible to show that the DG solution $\boldsymbol{U}^h$ of Eq. (5) with the associated boundary conditions must satisfy

$$B_{\mathrm{DG}}(\boldsymbol{V}, \boldsymbol{U}^h) = L_{\mathrm{DG}}(\boldsymbol{V}, \overline{\boldsymbol{B}}) \tag{9}$$

for any $\boldsymbol{V} \in (\mathcal{V}^{hp})^{N_u}$, where

$$\begin{aligned} B_{\mathrm{DG}}(\boldsymbol{V}, \boldsymbol{U}^h) &\equiv \int_{D^h} \left[\frac{\mathrm{d}\boldsymbol{V}^\intercal}{\mathrm{d}x_2}\left(\boldsymbol{Q}\frac{\mathrm{d}\boldsymbol{U}^h}{\mathrm{d}x_2} + \boldsymbol{R}\,\boldsymbol{U}^h\right) + \boldsymbol{V}^\intercal\left(\boldsymbol{R}^\intercal\frac{\mathrm{d}\boldsymbol{U}^h}{\mathrm{d}x_2} + \boldsymbol{S}\,\boldsymbol{U}^h\right)\right]\mathrm{d}x_2 + \\ &- \sum_{x_2 \in I^h}\left(\llbracket\boldsymbol{V}\rrbracket^\intercal\left\{\boldsymbol{Q}\frac{\mathrm{d}\boldsymbol{U}^h}{\mathrm{d}x_2} + \boldsymbol{R}\,\boldsymbol{U}^h\right\} + \left\{\frac{\mathrm{d}\boldsymbol{V}^\intercal}{\mathrm{d}x_2}\boldsymbol{Q} + \boldsymbol{V}^\intercal\boldsymbol{R}^\intercal\right\}\llbracket\boldsymbol{U}^h\rrbracket\right) \\ &+ \sum_{x_2 \in I^h} \mu\llbracket\boldsymbol{V}\rrbracket^\intercal\llbracket\boldsymbol{U}^h\rrbracket \\ &- \left(\nu_{x_2}\boldsymbol{V}^\intercal\left(\boldsymbol{Q}\frac{\mathrm{d}\boldsymbol{U}}{\mathrm{d}x_2} + \boldsymbol{R}\,\boldsymbol{U}\right) + \left(\frac{\mathrm{d}\boldsymbol{V}^\intercal}{\mathrm{d}x_2}\boldsymbol{Q} + \boldsymbol{V}^\intercal\boldsymbol{R}^\intercal\right)\boldsymbol{U}^h\nu_{x_2}\right)_{x_2=0} \\ &+ \left(\mu\boldsymbol{V}^\intercal\boldsymbol{U}^h\right)_{x_2=0} \end{aligned} \tag{10}$$

and

$$L_{\mathrm{DG}}(\boldsymbol{V}, \overline{\boldsymbol{B}}) \equiv \int_{D^h} \boldsymbol{V}^\intercal\overline{\boldsymbol{B}}\,\mathrm{d}x_2. \tag{11}$$

In Eqs. (10) and (11), the terms $\{\bullet\}$ and $\llbracket\bullet\rrbracket$ denotes the so-called average and jump operators, defined as

$$\{\bullet\} \equiv \frac{1}{2}(\bullet^e + \bullet^{e+1}) \quad \text{and} \quad \llbracket\bullet\rrbracket \equiv \bullet^e - \bullet^{e+1}, \tag{12}$$

the term $\int_{D^h} \bullet\,\mathrm{d}x_2 \equiv \sum_e \int_{D^e} \bullet\,\mathrm{d}x_2$ denotes the so-called broken integral, I^h is the set of inter-element interfaces, and ν_{x_2} is the element's outward unit normal. Note that, being the beam model one-dimensional, $\nu_{x_2}^e = -1$ and $\nu_{x_2}^e = +1$ for $x_2 = y_-^e$ and $x_2 = y_+^e$, respectively, where y_-^e and y_+^e are the two end points of the e-th element.

2.4. Discrete structural equations

Upon numerical integration and elemental assembly, the DG formulation produces a discrete system of the form

$$\mathbf{K}_\mathrm{S}\mathbf{X} = \mathbf{F} \tag{13}$$

where $\mathbf{K}_\mathrm{S}$ the structural stiffness matrix, the vector $\mathbf{X}$ collects the nodal components of the generalized displacements $\boldsymbol{U}\left(x_2\right)$ and $\mathbf{F}$ collects the components of the nodal forces. How it will be further discussed, in the considered aeroelastic case the loading term $\mathbf{F}$ depends on the aerodynamic flow, which in turn depends on the wing deformation itself, so that a suitable aerodynamic equation must be used to mathematically close the problem.

3. Aerodynamic model

The aerodynamic loads are computed using the vortex lattice method [27,36,37]. In the adopted VLM aerodynamic representation, analogous to those used e.g. in Refs. [38,39], the wing, subject to an aerodynamic flow with free-stream velocity $\mathbf{V}_\infty$, is replaced by a lifting surface, subdivided into a collection of non-overlapping *ring vortices*, while the wing wake is replaced by a set of *horseshoe vortices* shed by the wing trailing edge.

Two different vortex configurations are considered: *i*) the *planar* configuration, in which the lifting surface is defined by the geometric surface containing the chord lines of the wing airfoils, see Fig. 2a;

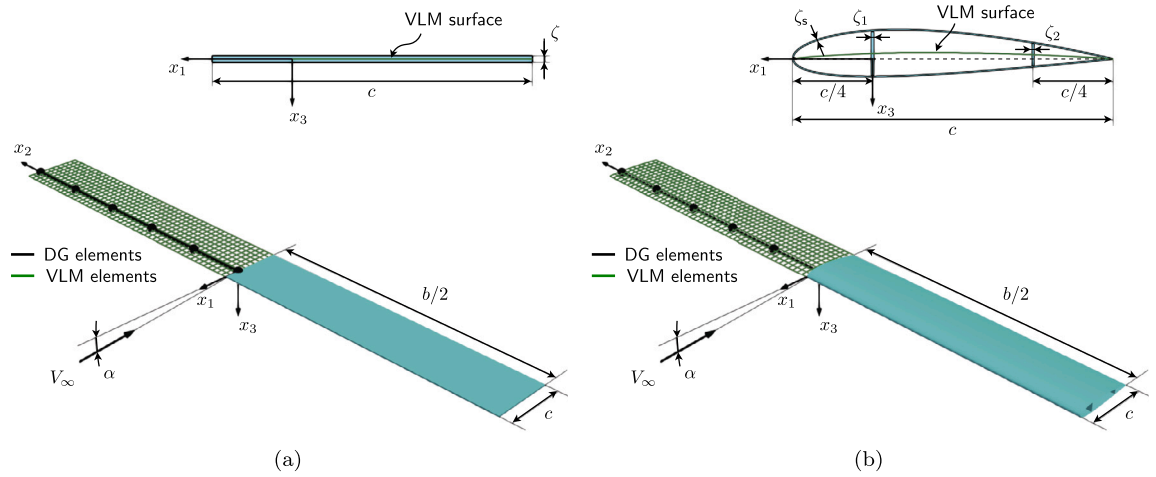

Fig. 2. (a) Planar DG-VLM configuration: the lifting surface is *flat* and contains the chord lines of the airfoils; (b) Non-planar DG-VLM configuration: the lifting surface contains the mean camber lines of the airfoils and features local curvature. (For interpretation of the colours in the figure(s), the reader is referred to the web version of this article.)

ii) the *non-planar* configuration, in which the lifting surface is defined by the geometric surface containing the mean camber lines of the wing airfoils, see Fig. 2b. In both cases, no twist is considered in the current implementation. The planar configuration is suitable for the aeroelastic analysis of flat plates subject to aerodynamic flows, while the non-planar model represents more accurately the case of aircraft wings, whose cross-sections are generally non-symmetric airfoils. It is however stressed that, also in the non-planar configuration, the vortex segments are piece-wise straight and do not feature any curvature. Therefore, there is no difference between the planar and non-planar cases in terms of practical implementation.

VLM is implemented in the same reference system $Ox_1x_2x_3$ as that used for the structural model and leads to a discrete system of aerodynamic equations of the form

$$\mathbf{A}(\mathbf{X})\boldsymbol{\Gamma} = \mathbf{b}(\mathbf{X}), \tag{14}$$

where $\boldsymbol{\Gamma}$ collects the unknown strengths of the attached ring and trailing horseshoe vortices and $\mathbf{A}(\mathbf{X})$ and $\mathbf{b}(\mathbf{X})$ are aerodynamic matrix terms stemming from the enforcement, at the lattice control points, of the aerodynamic impenetrability condition, which involves the velocity field resulting from the superposition of induced and free-stream velocities. The dependence of the aerodynamic solution on the structural deformation is reflected by the presence of the vector $\mathbf{X}$, introduced in Eq. (13), which affects both $\mathbf{A}$ and $\mathbf{b}$.

Once a solution for the vortex strengths $\boldsymbol{\Gamma}$ is available, the aerodynamic forces can be computed, as customary, by applying the Kutta-Joukowski lift theorem to the attached ring vortices. The aerodynamic force $\mathbf{F}_k$, acting on the *k-th* ring vortex, with leading edge vector segment $\mathbf{l}_k$ and strength Γ_k, computed as

$$\mathbf{F}_k = \rho_\infty \mathbf{V}_\infty \times \left(\Gamma_k \mathbf{l}_k\right) \qquad \rightarrow \qquad \mathbf{F}_{\mathsf{A}}(\boldsymbol{\Gamma}) \tag{15}$$

contributes to the population of the structural load vector $\mathbf{F}_A(\boldsymbol{\Gamma})$, depending on the aerodynamic solution, which acts as a body force term in the structural model.

The adopted implementation of VLM currently considers only steady incompressible aerodynamics; VLM, however, can be extended to take into account the presence of viscosity and compressibility effects and to model quasi-steady and unsteady problems, as done for example in Refs. [38,40]. Further extensions of VLM, considering also turbulence and other dissipative phenomena, are reported in the review in Ref. [41], where the *vortex particle method* for rotor blades is discussed.

4. Aeroelastic coupling

As previously mentioned, the aerodynamic forces acting on the structure depend on the deformation of the structure itself, which is in turn induced and affected by the aerodynamic loads themselves. The problem is thus inherently coupled.

In general, it may be assumed that both aerodynamic forces $\mathbf{F}_{\mathsf{A}}$ and non-aerodynamic forces $\mathbf{F}_{\mathsf{S}}$, e.g. weight, act on the structure. Recalling the form of Eqs. (13), (14), (15), the system governing the coupled aeroelastic system may be written as

$$\begin{cases} \mathbf{A}(\mathbf{X})\boldsymbol{\Gamma} = \mathbf{b}(\mathbf{X}) \\ \mathbf{K}_{\mathsf{S}}\mathbf{X} = \mathbf{F}_{\mathsf{S}} + \mathbf{F}_{\mathsf{A}}(\boldsymbol{\Gamma}) \end{cases} \tag{16}$$

where the aeroelastic coupling is explicitly reflected both by the dependency of the VLM coefficients on $\mathbf{X}$ and on the dependency of the aerodynamic forces on $\boldsymbol{\Gamma}$.

The aeroelastic system in Eq. (16) may be solved adopting different schemes, at different levels of accuracy. In this study, three different kinds of analysis are considered.

Static structural analysis (SSA): the aerodynamic forces are computed at the beginning of the analysis, considering the structure in the pristine configuration, and are applied on the structure, whose deformation is then computed only once, without subsequently considering the aerodynamic load redistribution. This corresponds to solving the one-way coupled system

$$\begin{cases} \mathbf{A}_0\boldsymbol{\Gamma}_0 = \mathbf{b}_0 \\ \mathbf{K}_{\mathsf{S}}\mathbf{X} = \mathbf{F}_{\mathsf{S}} + \mathbf{F}_{\mathsf{A}}(\boldsymbol{\Gamma}_0) \end{cases} \tag{17}$$

where $\mathbf{A}_0 \equiv \mathbf{A}(\mathbf{X}=\mathbf{0})$ and $\mathbf{b}_0 \equiv \mathbf{b}(\mathbf{X}=\mathbf{0})$. This kind of analysis would represent the first iteration of a staggered approach and it is considered for validation purposes, as several SSA results are available in the literature.

Linearly coupled static aeroelastic analysis ($\mathsf{SAA}_{\mathsf{LC}}$): it corresponds to solving the following linearisation of the aeroelastic system in Eq. (16)

$$\begin{cases} \mathbf{A}_0\boldsymbol{\Gamma} = \mathbf{b}_0 + \left.\dfrac{\partial \mathbf{b}}{\partial \mathbf{X}}\right|_{\mathbf{X}=\mathbf{0}} \mathbf{X} \\ \mathbf{K}_{\mathsf{S}}\mathbf{X} = \mathbf{F}_{\mathsf{S}} + \left.\dfrac{\partial \mathbf{F}_{\mathsf{A}}}{\partial \boldsymbol{\Gamma}}\right|_{\mathbf{X}=\mathbf{0}} \boldsymbol{\Gamma} \end{cases} \tag{18}$$

which, after some algebraic manipulation, leads to the aeroelastic system

$$\mathbf{K}_{\mathsf{AE}}\mathbf{X} = \mathbf{F}_{\mathsf{AE}} \tag{19}$$

with

$$\mathbf{K}_{\mathsf{AE}} \equiv \mathbf{K}_{\mathsf{S}} - \left.\frac{\partial \mathbf{F}_{\mathsf{A}}}{\partial \mathbf{\Gamma}}\right|_{\mathbf{X}=\mathbf{0}} \mathbf{A}_0^{-1} \left.\frac{\partial \mathbf{b}}{\partial \mathbf{X}}\right|_{\mathbf{X}=\mathbf{0}} \quad \text{and}$$

$$\mathbf{F}_{\mathsf{AE}} \equiv \mathbf{F}_{\mathsf{S}} + \left.\frac{\partial \mathbf{F}_{\mathsf{A}}}{\partial \mathbf{\Gamma}}\right|_{\mathbf{X}=\mathbf{0}} \mathbf{A}_0^{-1}\mathbf{b}_0. \tag{20}$$

The linearisation in Eq. (18) corresponds to approximating the aerodynamic impenetrability condition at the VLM control points $\boldsymbol{x}_c$ as

$$\left(\boldsymbol{v}_{ind} + \mathbf{V}_\infty\right) \cdot \boldsymbol{n} \approx \boldsymbol{v}_{ind} \cdot \boldsymbol{n}_0 + \mathbf{V}_\infty \cdot \boldsymbol{n} \tag{21}$$

where $\boldsymbol{n}_0$ and $\boldsymbol{n}$ represent the unit normals at the control points over the lifting surface, in the undeformed and deformed configuration respectively. In particular, the consideration of the zero-*th* term only in the linearisation of $\mathbf{A}(\mathbf{X})$ corresponds to considering the projection of the induced velocity $\boldsymbol{v}_{ind}$ with respect to the undeformed normals, as indicated by the first term in the right-hand side of Eq. (21). This case is considered here, as it is often assumed as a standard approximation in several literature works.

Non-linearly coupled static aeroelastic analysis ($\mathsf{SAA}_{\mathsf{NLC}}$): it corresponds to exactly solving the aeroelastic system in Eq. (16), e.g. using a Newton-Raphson solver with initial guess corresponding to the undeformed structural configuration.

It is worth highlighting that the above SAA schemes are referred to as *linear* or *non-linear* with reference to the mathematical representation of the aeroelastic coupling. In any case, the structural model is linear, as only small strains are considered. It will be shown, in Section 5, how the linearly-coupled and the non-linearly coupled solutions differ only for wings featuring high aspect ratios, which would probably demand a large-strain structural model for the accurate representation of the structural deformation.

5. Numerical results

The proposed numerical scheme has been implemented into an in-house code. The present section is devoted to its assessment and validation with respect to available literature data.

Before assessing the coupled aeroelastic formulation, the implemented VLM has been preliminarily successfully tested, reproducing classical results about the spanwise distribution of the section lift coefficient, as those reported e.g. in Refs. [27,42,24]. All the tests reported in the subsequent sections have thus been performed with a fixed VLM grid consisting of 10×50 vortices, of which 9×50 attached ring vortices (50 along the span and 9 along the chordline) and 50 horseshoe trailing vortices.

On the other hand, the generic DG structural model is identified by *both* the acronym BT_N, where BT stands for *beam theory* and N is the order of expansion of the fields over the beam transverse section, *and* the parameter p, which expresses the order of the polynomial approximation of $\boldsymbol{U}\left(x_2\right)$ along the beam span in Eq. (3). Further specifying Eq. (3), it is worth noting that an expansion of order N and p of the generic displacement component u_k, $k = 1, 2, 3$, is given by

$$u_k\left(x_1, x_2, x_3\right) = \sum_{m,n=0}^{N} \sum_{q=0}^{p} P_m\left(x_1\right) P_n\left(x_3\right) P_q\left(x_2\right) X_{mnq} \tag{22}$$

where P_r is the Legendre polynomial of order r scaled with respect to the relevant geometric reference length, namely the chord for $P_m\left(x_1\right)$, the plate or airfoil thickness for $P_n\left(x_3\right)$ or the element span-wise length for $P_q\left(x_2\right)$. The number of degrees of freedom associated with the chosen structural model is thus $\mathsf{DOF} = 3\left(1+p\right)\left(1+N\right)^2 N_{el}$, with N_{el} expressing the number of DG elements along the span of the wing.

5.1. Wings with flat-plate cross section

The first set of tests considers a cantilever untapered flat plate subject to a steady aerodynamic flow, according to the problem setup sketched in Fig. 2a.

In this and in all the subsequent tests the structure is made of an isotropic and homogeneous elastic material with Young's modulus $E = 69\,\mathrm{GPa}$ and Poisson's ratio $\nu = 0.33$, so to reproduce the results presented in Ref. [42]. The plate has chord $c = 1\,\mathrm{m}$ while its span b and thickness ζ are varied throughout the tests. The air density has been assumed as $\rho_\infty = 1.225\,\mathrm{kg\,m^{-3}}$ in all the tests, while the free-stream velocity V_∞ and the angle of attack α span different values in the investigation.

Fig. 3 shows the convergence behaviour of the aeroelastic model, in terms of wing tip maximum deflection $u_z|_{\mathrm{tip}}$ and wing tip twist $\Delta u_z|_{\mathrm{tip}} = u_z|_{\mathrm{tip}}^{LE} - u_z|_{\mathrm{tip}}^{TE}$, with respect to the number of degrees of freedom of the DG beam model, for BT_3 and different orders of polynomial approximation p in Eq. (3) or in Eq. (22). Also, the different coupling schemes described in Section 4 – SSA, $\mathsf{SAA}_{\mathsf{LC}}$ and $\mathsf{SAA}_{\mathsf{NLC}}$ – are tested. In this test, the Wing/plate geometry is specified by $b/2 = 5\,\mathrm{m}$ and $\zeta = 0.02\,\mathrm{m}$, while the initial angle of attack is $\alpha = 1^\circ$. In general it can be observed that: *i*) the convergence with respect to the number of DoFs, which in the considered application is directly linked with the number of DG elements along the wing span, improves as p increases; *ii*) both the $\mathsf{SAA}_{\mathsf{LC}}$ and $\mathsf{SAA}_{\mathsf{NLC}}$ schemes produce very similar results for the considered structure, which differ, as expected, from the results provided by the SSA, which in this case correspond to a lower tip deflection and twist.

Fig. 4 investigates the behaviour of the same flat wing as that considered in the previous test at increasing values of free-stream velocity V_∞. In particular, the wing-tip twist curves $\Delta u_z|_{\mathrm{tip}} = f\left(V_\infty\right)$, as obtained from a structural model comprised of 5 DG elements with BT_3 and $p = 5$, are plotted for the different coupling schemes discussed above. It is observed that: *i*) the present model provides results matching the literature references both in the case of SSA and SAA; *ii*) for the considered aspect ratio and test conditions there is no difference between the $\mathsf{SAA}_{\mathsf{LC}}$ and $\mathsf{SAA}_{\mathsf{NLC}}$ solution schemes.

The difference between the SSA and SAA responses is even more evident when the free-stream velocity approaches the divergence speed V_D, which is computed solving the following eigenvalue problem associated with Eq. (19)

$$\left(\mathbf{K}_{\mathsf{S}} - \rho_\infty V_D^2 \left.\frac{\partial \widehat{\mathbf{F}}_{\mathsf{A}}}{\partial \mathbf{\Gamma}}\right|_{\mathbf{X}=\mathbf{0}} \mathbf{A}_0^{-1} \left.\frac{\partial \widehat{\mathbf{b}}}{\partial \mathbf{X}}\right|_{\mathbf{X}=\mathbf{0}}\right)\mathbf{X} = \mathbf{0}, \tag{23}$$

where $\widehat{\mathbf{b}}$ and $\widehat{\mathbf{F}}_{\mathsf{A}}$ correspond to computing $\mathbf{b}$ and $\mathbf{F}_{\mathsf{A}}$, respectively, upon assuming free-stream velocity $V_\infty = 1$ and free-stream density $\rho_\infty = 1$. The computed values of $\Delta u_z|_{\mathrm{tip}} = f\left(V_\infty\right)$ as V_∞ approaches V_D are displayed in Fig. 5 for the SSA and SAA cases. It is worth stressing that the results shown in Fig. 5 are obtained employing a linear structural model and do not account for geometric or material nonlinear effects. A departure from the curves shown in the figure would emerge and would be captured by a finite-strain formulation beyond a certain free-stream velocity threshold, in both the SSA and SAA cases. Finite-strain formulations can be accommodated in the developed DG-VLM framework and will be considered in future investigations.

Table 1 explores the effect on the solution of the order of expansion of the fields over the beam transverse section, i.e. of N in BT_N, at different values of the free-stream velocity V_∞. The wing is the same as that considered above, with $b/2 = 5\,\mathrm{m}$, $\zeta = 0.02\,\mathrm{m}$, and $\alpha = 1^\circ$. All results are compared, in terms of maximum wing tip deflection $u_z|_{\mathrm{tip}}$, with those reported in Ref. [24], for the $\mathsf{SAA}_{\mathsf{LC}}$ case. In all tests, 5 DG elements along the wing span, with $p = 5$, have been used. It can be observed that, for the analysed test case, the proposed model is almost insensitive to N, providing very similar results for all values of $N = 1, \ldots, 4$ at all the investigated values of free-stream velocity, differently

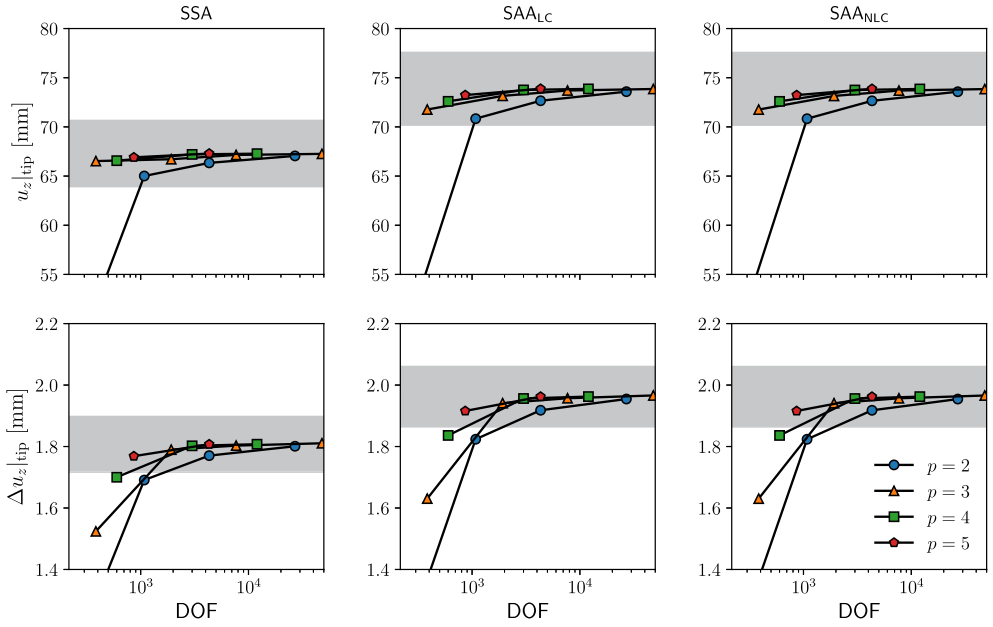

Fig. 3. Convergence of (*top*) the wing tip maximum deflection $u_z|_{tip}$ and (*bottom*) the wing tip twist $\Delta u_z|_{tip}$ with respect to the number of degrees of freedom for a cantilever flat plate subject to a uniform and constant aerodynamic flow. Wing/plate geometry: $b/2 = 5$ m and $\zeta = 0.02$ m. Free-stream conditions: $V_\infty = 30\,\mathrm{m\,s^{-1}}$ and $\alpha = 1^\circ$. Structural theory: BT$_3$. Analyses: (*left*) SSA, (*center*) SAA$_{LC}$, (*right*) SAA$_{NLC}$. The gray areas denote the region of less than 5% deviation from the converged value.

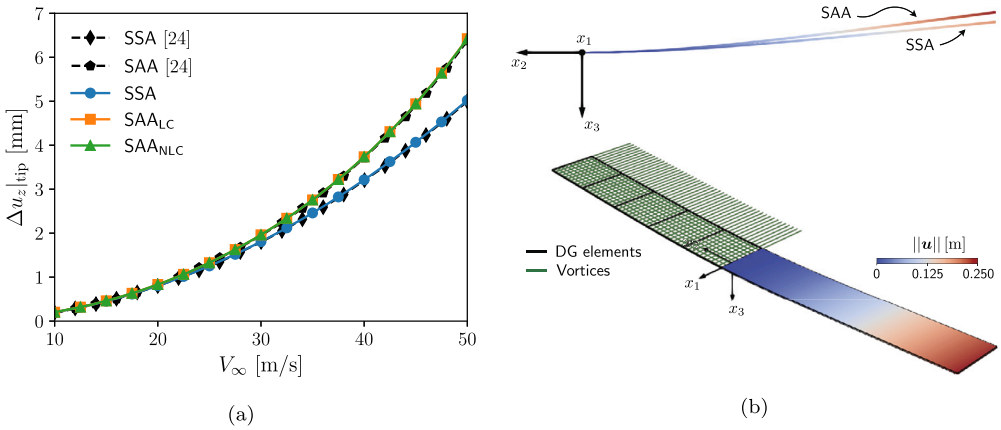

Fig. 4. (a) Wing tip twist $\Delta u_z|_{tip}$ as a function of the free-stream velocity V_∞. Wing geometry: $b/2 = 5$ m and $\zeta = 0.02$ m. Free-stream conditions: $\alpha = 1^\circ$. Structural theory: BT$_3$. Structural mesh: 1×5. Polynomial order: $p = 5$. (b) Schematic of the considered aeroelastic model showing the VLM computational grid (*green*), the DG structural grid (*black*), a representation of the computed displacements over the wing and a frontal view of the deformed wing, highlighting the difference between the SSA and SAA solutions. (For interpretation of the colours in the figure(s), the reader is referred to the web version of this article.)

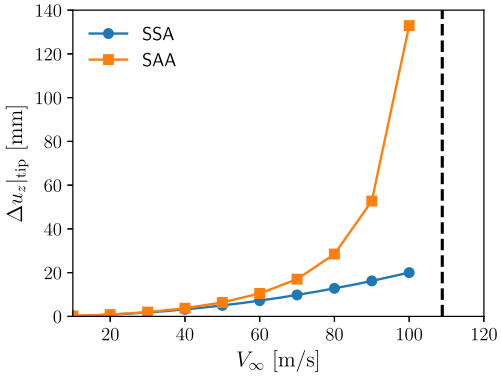

Fig. 5. Wing tip twist $\Delta u_z|_{tip}$ as a function of the free-stream velocity V_∞ approaching the divergence speed (the dashed line).

from what observed in the reference literature. The converged values match very well with those provided by NASTRAN in Ref. [24].

Table 2 reports the values of the maximum wing tip deflection $u_z|_{tip}$ at different values of wing span b, as computed by employing different orders of expansion N in BT$_N$ and different aeroelastic coupling schemes, i.e. SSA, SAA$_{LC}$ and SAA$_{NLC}$. In all cases $\zeta = 0.1$ m, $V_\infty = 70\,\mathrm{m\,s^{-1}}$, $\alpha = 1^\circ$, and 1×5 DG structural elements along the wing span are used, with polynomial order $p = 5$.

It can be observed that, for the shortest wing, both the order of expansion N and the coupling scheme have little effect on the obtained result, which is also satisfyingly close to the reference literature data and the NASTRAN output. In particular, the convergence can be considered already attained for $N = 1$ and the aeroelastic solution is naturally slightly different from the static structural one, but not influenced by the linear or non-linear nature of the aeroelastic coupling equations.

Table 1
Wing tip maximum deflection $u_z|_{\text{tip}}$ provided by different structural theories BT_N at different values of the free-stream velocity V_∞. Wing geometry: $b/2 = 5\,\text{m}$ and $\zeta = 0.02\,\text{m}$. Free-stream conditions: $\alpha = 1^\circ$. Structural mesh: 1×5 (5 1D elements along the span). Polynomial order: $p = 5$. Reference and NASTRAN values are taken from Ref. [24].

	$u_z\|_{\text{tip}}$ [mm]								
V_∞	BT_1		BT_2		BT_3		BT_4		
[m/s]	Ref.	Present	Ref.	Present	Ref.	Present	Ref.	Present	NASTRAN
10	7.6275	7.5616	7.0244	7.5519	7.4966	7.5524	7.5126	7.5527	7.5446
30	68.622	73.973	68.236	73.869	73.241	73.878	73.397	73.880	73.731
50	190.48	247.08	224.45	246.67	243.94	246.73	244.96	246.74	245.49

Table 2
Wing tip maximum tip deflection $u_z|_{\text{tip}}$ as a function of the wing span b for different structural theories and aeroelastic coupling schemes. Wing geometry: $\zeta = 0.1\,\text{m}$. Free-stream conditions: $V_\infty = 70\,\text{m s}^{-1}$ and $\alpha = 1^\circ$. Structural mesh: 1×5. Polynomial order: $p = 5$. Reference and NASTRAN values are taken from Ref. [24].

		$u_z\|_{\text{tip}}$ [mm]								
$b/2$		BT_1		BT_2		BT_3		BT_4		
[m]		Ref.	Present	Ref.	Present	Ref.	Present	Ref.	Present	NASTRAN
5	SSA	2.9928	2.9499	2.8620	2.9324	2.9192	2.9340	2.9325	2.9361	-
	SAA_{LC}	2.9933	2.9622	2.8731	2.9445	2.9307	2.9462	2.9443	2.9483	2.9505
	SAA_{NLC}		2.9622		2.9445		2.9462		2.9483	
10	SSA	56.366	55.671	54.631	55.426	55.358	55.438	55.478	55.470	-
	SAA_{LC}	56.402	56.845	55.717	56.585	56.465	56.605	56.611	56.637	56.723
	SAA_{NLC}		56.845		56.585		56.605		56.637	
20	SSA	1000.3	990.83	981.43	987.73	988.76	987.87	989.72	988.21	-
	SAA_{LC}	1003.0	1091.8	1075.8	1087.6	1084.1	1088.4	1087.3	1088.8	1092.8
	SAA_{NLC}		1089.6		1085.4		1086.2		1086.6	

As b and thus the wing aspect ratio increase though, see e.g. the case $b/2 = 20\,\text{m}$, the importance of the aeroelastic coupling becomes more relevant, as highlighted by the more pronounced differences between the SSA, SAA_{LC} and SAA_{NLC} solutions. On the other hand, a satisfying convergence is already attained for $N = 2$. For the longest wing, a satisfying match with the reference data is attained.

5.2. Wings with NACA airfoil cross section

The second test considers a straight untapered and untwisted wing, featuring a thin-walled NACA 2415 airfoil made of aluminum, with $E = 69\,\text{GPa}$ and Poisson's ratio $\nu = 0.33$. The problem setup is sketched in Fig. 2b, where the airfoil shape is generated employing the analytical expressions of the camber and thickness distribution functions associated with four-digit NACA airfoils. Several tests, mimicking what has been done for the flat plate wing, have been performed, reaching similar conclusions. Here, the comparison with the results reported in Ref. [24] are presented.

A wing with NACA 2415 airfoil, chord $c = 1\,\text{m}$, span $b = 5\,\text{m}$, subject to a free stream with $V_\infty = 50\,\text{m s}^{-1}$ and $\alpha = 3^\circ$ is considered. Table 3 reports the results provided by both the SSA and SAA_{LC} schemes, employing both the planar and non-planar VLM implementations for the aerodynamics. A satisfying agreement between the results obtained using the planar VLM implementation and the reference literature data is recorded, in terms of wing tip maximum tip deflection $u_z|_{\text{tip}}$. The results obtained employing the non-planar VLM are slightly higher, which appears physically consistent considering that the non planar vortex representation captures the effect of the airfoil curvature, neglected in the planar VLM implementation.

Table 3
Wing tip maximum deflection for the SSA and the SAA_{LC} cases. Wing geometry: airfoil-shaped wing, NACA 2415. Free-stream conditions: $V_\infty = 5\,\text{m s}^{-1}$ and $\alpha = 3^\circ$. Structural mesh: 1×5. Structural theory: BT_4. Polynomial order: $p = 5$.

	$u_z\|_{\text{tip}}$ [mm]		
	Ref. [24]	Present	
		Flat VLM $\alpha_0 = 0$	Curved VLM $\alpha_0 = -2.1396^\circ$
SSA	8.6854	8.8967	9.2117
SAA_{LC}	8.8377	8.9159	9.2018

6. Discussion

This paper presents a novel computational framework for static aeroelasticity. The novelty consists in the use of an original discontinuous Galerkin formulation for resolving the structural response of the wing, coupled with a vortex lattice method for capturing the aerodynamic loading.

The structural model combines generalized kinematic assumptions, as in CUFs [29] or GUFs [14], with the high order and tunable accuracy granted by the discontinuous Galerkin solution of the resulting governing equations. The use of generalized kinematics is particularly suitable for the analysis of structural components featuring cross sections of general complexity, e.g. including the presence of spars and stringers, as it is often the case in the analysis of wing structures, as shown in Refs. [15,16]. On the other hand, the use of the DG technique offers several advantages over alternative approaches such as FEM. In particular, being based on the use of discontinuous local basis functions and weakly enforced boundary and inter-element continuity conditions, the method: *i*) naturally provides high order accuracy in the interpolation of the problem fields, including the possibility of using different orders of approximation over different mesh elements, with subsequent reduction in the number of DoF needed to achieve a desired approximation, as demonstrated in Ref. [28]; *ii*) enables seamless computing parallelization of the integration and assembly routines for the population of the discrete operators, e.g. the stiffness matrix, which becomes attractive in large scale problems; *iii*) allows straightforward coupling

with other techniques in multi-field analyses, which is here employed for the construction of the fluid-structure interface.

In this work, the DG structural model has been coupled with both planar and non-planar implementations of the VLM as the model of choice for capturing stationary aerodynamic flows over the wing. The coupled structural-aerodynamic model has proven able to capture the static aeroelastic behaviour of the wing, providing accurate results in terms of wing deformation with respect to reference literature data.

However, following the successful validation of the proposed framework for considered set of benchmark tests, several directions of further investigation can be identified. From the structural point of view, the tool can be extended to considering more complex structural and/or material configurations, e.g. composite wings, including *variable angle tow* configurations, with more realistic inclusion of stiffeners, ribs and cut-outs [30,32,34,43,15,16]. Another interesting structural development could be addressed at including large-strain kinematics, which would render the tool suitable for the analysis of flexible aircraft, e.g. MALE or HALE unmanned aircraft platforms [44]. Remaining with the domain of static problems, the aerodynamic component of the model could be extended to include the analysis of compressible flows [45]

On the other hand, the inclusion of structural dynamics, which is straightforward within the proposed DG model, and of unsteady aerodynamics, e.g. through either unsteady VLM [23] or *doublet lattice method* [46] would ope to the analysis of flutter aeroelastic problems.

Considering the proven capability of the DG model to analyse complex laminated and multi-functional structures [33,47], the inclusion of large strains, dynamics and the modelling of highly stretchable multifunctional materials, through e.g. hyper-elastic constitutive laws, would provide a tool for the analysis of fluid-structure interaction energy harvesting devices [48,49].

7. Conclusions

In this work, an original computational framework for the static aeroelastic analysis of wings has been developed, tested and validated. The novelty of the formulation is the use of a discontinuous Galerkin formulation for modelling wing structures that has been coupled with a Vortex Lattice method for modelling lifting surfaces.

Two types of wing structures have been considered, namely a wing with a flat-plate cross section and a wing with an airfoil-shaped, thin-walled cross sections. The effect of the model parameters, such as the kinematic approximation and the order of the DG interpolation, as well as the effect of the problem parameters, such as the wing aspect ratio and free-stream velocity, on the deflection and twisting of the wing tip have been presented and discussed. The comparison between the obtained results and those available in the literature confirms the accuracy and capability of the present framework.

Declaration of competing interest

We have no known competing financial interests or personal relationships that could have appeared to influence the work reported in this paper.

Data availability

Data will be made available on request.

Acknowledgements

This work has been supported by the European Union - NextGenerationEU - MUR D.M. 737/2021 funds through the Project EUROSTART ClearWay (PRJ-0993) at the University of Palermo.

References

[1] T. Wu, A. Kareem, Y. Ge, Linear and nonlinear aeroelastic analysis frameworks for cable-supported bridges, Nonlinear Dyn. 74 (2013) 487–516, https://doi.org/10.1007/s11071-013-0984-7.
[2] H. Dongmei, Z. Ledong, D. Quanshun, Z. Xue, C. Wei, Aeroelastic and aerodynamic interference effects on a high-rise building, J. Fluids Struct. 69 (2017) 355–381, https://doi.org/10.1016/j.jfluidstructs.2017.01.007.
[3] P. Zhang, S. Huang, Review of aeroelasticity for wind turbine: current status, research focus and future perspectives, Front. Energy 5 (2011) 419–434, https://doi.org/10.1007/s11708-011-0166-6.
[4] R.M. Ajaj, M.S. Parancheerivilakkathil, M. Amoozgar, M.I. Friswell, W.J. Cantwell, Recent developments in the aeroelasticity of morphing aircraft, Prog. Aerosp. Sci. 120 (2021) 100682, https://doi.org/10.1016/j.paerosci.2020.100682.
[5] A. Larsen, Aerodynamics of the Tacoma Narrows Bridge - 60 years later, Struct. Eng. Int. 10 (4) (2000) 243–248, https://doi.org/10.2749/101686600780481356.
[6] G. Arioli, F. Gazzola, Torsional instability in suspension bridges: the Tacoma Narrows Bridge case, Commun. Nonlinear Sci. Numer. Simul. 42 (2017) 342–357, https://doi.org/10.1016/j.cnsns.2016.05.028.
[7] M.H. Hansen, Aeroelastic instability problems for wind turbines, Wind Energy 10 (6) (2007) 551–577, https://doi.org/10.1002/we.242.
[8] J. Hao, T. Wu, Downburst-induced transient response of a long-span bridge: a cfd-csd-based hybrid approach, J. Wind Eng. Ind. Aerodyn. 179 (2018) 273–286, https://doi.org/10.1016/j.jweia.2018.06.006.
[9] M. Ilie, A fully-coupled cfd/csd computational approach for aeroelastic studies of helicopter blade-vortex interaction, Appl. Math. Comput. 347 (2019) 122–142, https://doi.org/10.1016/j.amc.2018.10.069.
[10] D.O. Yu, O.J. Kwon, Predicting wind turbine blade loads and aeroelastic response using a coupled cfd–csd method, in: Special Issue on Aerodynamics of Offshore Wind Energy Systems and Wakes, Renew. Energy 70 (2014) 184–196, https://doi.org/10.1016/j.renene.2014.03.033.
[11] H.H. Mian, G. Wang, Z.-Y. Ye, Numerical investigation of structural geometric nonlinearity effect in high-aspect-ratio wing using cfd/csd coupled approach, J. Fluids Struct. 49 (2014) 186–201, https://doi.org/10.1016/j.jfluidstructs.2014.04.011.
[12] L. Wang, X. Liu, A. Kolios, State of the art in the aeroelasticity of wind turbine blades: aeroelastic modelling, Renew. Sustain. Energy Rev. 64 (2016) 195–210, https://doi.org/10.1016/j.rser.2016.06.007.
[13] M. Sayed, P. Bucher, G. Guma, T. Lutz, R. Wüchner, Aeroelastic simulations based on high-fidelity cfd and csd models, Handb. Wind Energy Aerodyn. (2022) 1–76, https://doi.org/10.1007/978-3-030-05455-7_22-1.
[14] L. Demasi, Y. Ashenafi, R. Cavallaro, E. Santarpia, Generalized unified formulation shell element for functionally graded variable-stiffness composite laminates and aeroelastic applications, Compos. Struct. 131 (2015) 501–515, https://doi.org/10.1016/j.compstruct.2015.05.022.
[15] M. Grifò, A. Da Ronch, I. Benedetti, A computational aeroelastic framework based on high-order structural models and high-fidelity aerodynamics, Aerosp. Sci. Technol. 132 (2023) 108069, https://doi.org/10.1016/j.ast.2022.108069.
[16] M. Grifò, V. Gulizzi, A. Milazzo, A. Da Ronch, I. Benedetti, High-fidelity aeroelastic transonic analysis using higher-order structural models, Compos. Struct. 321 (2023) 117315, https://doi.org/10.1016/j.compstruct.2023.117315.
[17] G.P. Guruswamy, Computational-fluid-dynamics- and computational-structural-dynamics-based time-accurate aeroelasticity of helicopter rotor blades, J. Aircr. 47 (3) (2010) 858–863, https://doi.org/10.2514/1.45744.
[18] M. Sayed, T. Lutz, E. Krämer, S. Shayegan, A. Ghantasala, R. Wüchner, K.-U. Bletzinger, High fidelity cfd-csd aeroelastic analysis of slender bladed horizontal-axis wind turbine, J. Phys. Conf. Ser. 753 (4) (2016) 042009, https://doi.org/10.1088/1742-6596/753/4/042009.
[19] M. Smith, M. Patil, D. Hodges, Cfd-based analysis of nonlinear aeroelastic behavior of high-aspect ratio wings, in: 19th AIAA Applied Aerodynamics Conference, 2001, p. 1582.
[20] S. Munteanu, J. Rajadas, C. Nam, A. Chattopadhyay, Reduced-order-model approach for aeroelastic analysis involving aerodynamic and structural nonlinearities, AIAA J. 43 (3) (2005) 560–571, https://doi.org/10.2514/1.10971.
[21] J. Kou, W. Zhang, A hybrid reduced-order framework for complex aeroelastic simulations, Aerosp. Sci. Technol. 84 (2019) 880–894, https://doi.org/10.1016/j.ast.2018.11.014.
[22] D. Li, A. Da Ronch, G. Chen, Y. Li, Aeroelastic global structural optimization using an efficient cfd-based reduced order model, Aerosp. Sci. Technol. 94 (2019) 105354, https://doi.org/10.1016/j.ast.2019.105354.
[23] J. Murua, R. Palacios, J.M.R. Graham, Applications of the unsteady vortex-lattice method in aircraft aeroelasticity and flight dynamics, Prog. Aerosp. Sci. 55 (2012) 46–72, https://doi.org/10.1016/j.paerosci.2012.06.001.
[24] E. Carrera, A. Varello, L. Demasi, A refined structural model for static aeroelastic response and divergence of metallic and composite wings, CEAS Aeronaut. J. 4 (2) (2013) 175–189.
[25] M. Petrolo, Flutter analysis of composite lifting surfaces by the 1D Carrera Unified Formulation and the doublet lattice method, Compos. Struct. 95 (2013) 539–546, https://doi.org/10.1016/j.compstruct.2012.06.021.
[26] C. Xie, L. Wang, C. Yang, Y. Liu, Static aeroelastic analysis of very flexible wings based on non-planar vortex lattice method, Chin. J. Aeronaut. 26 (3) (2013) 514–521, https://doi.org/10.1016/j.cja.2013.04.048.

[27] J. Katz, A. Plotkin, Low-Speed Aerodynamics, 2nd edition, Cambridge Aerospace Series, Cambridge University Press, 2001.
[28] V. Gulizzi, I. Benedetti, A. Milazzo, High-order accurate beam models based on discontinuous Galerkin methods, Aerotec. Missili Spaz. (2023) 1–16.
[29] E. Carrera, M. Cinefra, M. Petrolo, E. Zappino, Finite Element Analysis of Structures Through Unified Formulation, John Wiley & Sons, 2014.
[30] V. Gulizzi, I. Benedetti, A. Milazzo, A high-resolution layer-wise discontinuous Galerkin formulation for multilayered composite plates, Compos. Struct. 242 (2020) 112137.
[31] R.K. Kapania, Y. Liu, Static and vibration analyses of general wing structures using equivalent-plate models, AIAA J. 38 (7) (2000) 1269–1277, https://doi.org/10.2514/2.1098.
[32] V. Gulizzi, I. Benedetti, A. Milazzo, An implicit mesh discontinuous Galerkin formulation for higher-order plate theories, Mech. Adv. Mat. Struct. 27 (17) (2020) 1494–1508.
[33] G. Guarino, A. Milazzo, V. Gulizzi, Equivalent-single-layer discontinuous Galerkin methods for static analysis of multilayered shells, Appl. Math. Model. 98 (2021) 701–721.
[34] G. Guarino, V. Gulizzi, A. Milazzo, High-fidelity analysis of multilayered shells with cut-outs via the discontinuous Galerkin method, Compos. Struct. 276 (2021) 114499.
[35] G. Guarino, V. Gulizzi, A. Milazzo, Accurate multilayered shell buckling analysis via the implicit-mesh discontinuous Galerkin method, AIAA J. 60 (12) (2022) 6854–6868.
[36] M. Drela, Flight Vehicle Aerodynamics, MIT Press, 2014.
[37] J.J. Bertin, R.M. Cummings, Aerodynamics for Engineers, Cambridge University Press, 2021.
[38] O. Şugar Gabor, A. Koreanschi, R.M. Botez, A new non-linear vortex lattice method: applications to wing aerodynamic optimizations, Chin. J. Aeronaut. 29 (5) (2016) 1178–1195, https://doi.org/10.1016/j.cja.2016.08.001.
[39] C. Xie, C. An, L. Yi, Y. Chao, Static aeroelastic analysis including geometric nonlinearities based on reduced order model, Chin. J. Aeronaut. 30 (02 2017), https://doi.org/10.1016/j.cja.2016.12.031.
[40] M. Parenteau, F. Plante, E. Laurendeau, M. Costes, Unsteady coupling algorithm for lifting-line methods, in: 55th AIAA Aerospace Sciences Meeting, 2017, p. 0951.
[41] H. Lee, B. Sengupta, M. Araghizadeh, R. Myong, Review of vortex methods for rotor aerodynamics and wake dynamics, Adv. Aerodyn. 20 (4) (2022), https://doi.org/10.1186/s42774-022-00111-3.
[42] A. Varello, E. Carrera, L. Demasi, Vortex lattice method coupled with advanced one-dimensional structural models, J. Aeroelast. Struct. Dyn. 2 (2) (2011).
[43] I.B.D. Campagna, A. Milazzo, V. Oliveri, A non-linear Ritz method for progressive failure analysis of variable angle tow composite laminates, Mech. Adv. Mat. Struct. 30 (5) (2023) 995–1008, https://doi.org/10.1080/15376494.2022.2134951.
[44] R. Palacios, J. Murua, R. Cook, Structural and aerodynamic models in nonlinear flight dynamics of very flexible aircraft, AIAA J. 48 (11) (2010) 2648–2659, https://doi.org/10.2514/1.J050513.
[45] R. Palacios, C. Cesnik, Static nonlinear aeroelasticity of flexible slender wings in compressible flow, in: 46th AIAA/ASME/ASCE/AHS/ASC Structures, Structural Dynamics and Materials Conference, 2005, p. 1945.
[46] E. Albano, W.P. Rodden, A doublet-lattice method for calculating lift distributions on oscillating surfaces in subsonic flows, AIAA J. 7 (2) (1969) 279–285, https://doi.org/10.2514/3.5086.
[47] I. Benedetti, V. Gulizzi, A. Milazzo, Layer-wise discontinuous Galerkin methods for piezoelectric laminates, Modelling 1 (2) (2020) 198–214, URL, https://www.mdpi.com/2673-3951/1/2/12.
[48] J. De Marqui Carlos, W.G.R. Vieira, A. Erturk, D.J. Inman, Modeling and analysis of piezoelectric energy harvesting from aeroelastic vibrations using the doublet-lattice method, J. Vib. Acoust. 133 (1) (2010) 011003.
[49] I. Collins, M. Hossain, W. Dettmer, I. Masters, Flexible membrane structures for wave energy harvesting: a review of the developments, materials and computational modelling approaches, Renew. Sustain. Energy Rev. 151 (2021) 111478, https://doi.org/10.1016/j.rser.2021.111478.